J. Space Weather Space Clim. 2022, **12**, 33

https://doi.org/10.1051/swsc/2022029

JSWSC

Available online at:
www.swsc-journal.org

Topical Issue - Ionospheric plasma irregularities and their impact on radio systems

RESEARCH ARTICLE OPEN ACCESS

The implications of ionospheric disturbances for precise GNSS positioning in Greenland

Jacek Paziewski[1,*], Per Høeg[2], Rafal Sieradzki[1], Yaqi Jin[2], Wojciech Jarmolowski[1], M. Mainul Hoque[3], Jens Berdermann[3], Manuel Hernandez-Pajares[4], Pawel Wielgosz[1], Haixia Lyu[4,5], Wojciech J. Miloch[2], and Raul Orús-Pérez[6]

[1] University of Warmia and Mazury in Olsztyn, Faculty of Geoengineering, Oczapowskiego 2, 10-719 Olsztyn, Poland
[2] University of Oslo, Department of Physics, PO Box 1048, Blindern, 0316 Oslo, Norway
[3] German Aerospace Center (DLR), Institute for Solar-Terrestrial Physics, Kalkhostweg 53, 17235 Neustrelitz, Germany
[4] Universitat Politecnica de Catalunya, Department of Mathematics, IonSAT, 08034 Barcelona, Spain
[5] Wuhan University, GNSS Research Center, Luoyu Road 129, Wuhan city, Hubei Province, PR China
[6] European Space Agency (ESA), Keplerlaan, 1, 2201AZ Noordwijk, ZH, The Netherlands

Received 4 March 2022 / Accepted 24 August 2022

Abstract – Ionospheric irregularities impair Global Navigation Satellite System (GNSS) signals and, in turn, affect the performance of GNSS positioning. Such effects are especially evident at low and high latitudes, which are currently gaining the attention of research and industry sectors. This study evaluates the impact of ionospheric irregularities on GNSS positioning in Greenland. We assess the performance of positioning methods that meet the demands of a wide range of users. In particular, we address the needs of the users of mass-market single-frequency receivers and those who require a solution of high precision provided by geodetic dual-frequency receivers. We take advantage of the datasets collected during three ionospheric storms: the St. Patrick's Day storm of March 17, 2015, the storm on June 22, 2015, and another on August 25–26, 2018. We discover a significant impact of the ionospheric disturbances on the ambiguity resolution performance and the accuracy of the float solution in Real Time Kinematics (RTK) positioning. Next, assessing the single-frequency ionosphere-free Precise Point Positioning (PPP), we demonstrate that the model is generally unaffected by ionospheric disturbances. Hence, the model is predestined for the application by the users of single-frequency receivers in the areas of frequent ionospheric disturbances. Finally, based on the observation analyses, we reveal that phase signals on the L2 frequency band are more prone to cycle slips induced by ionospheric irregularities than those transmitted on the L1. Such signal properties explain a noticeable decline in the dual-frequency RTK performance during the ionospherically disturbed period and merely no effect for the single-frequency ionosphere-free PPP model.

Keywords: Precise positioning / GNSS / ionospheric irregularities / RTK / PPP / Greenland

1 Introduction and motivation

Ionospheric irregularities are responsible for disrupting the Global Navigation Satellite System (GNSS) positioning performance in terms of accuracy, reliability, and availability (Hernandez-Pajares et al., 2011). In particular, such disturbances may induce cycle slips, loss of lock, and fluctuations of GNSS signals, as well as cause a deterioration in terms of signal-to-noise ratio, as proved in the following references (Ji et al., 2013; Andalsvik & Jacobsen, 2014; Muhammad et al., 2015; Prikryl et al., 2016). Thus, the evaluation of GNSS positioning performance under the presence of ionospheric disturbances has been the subject of several studies in recent years. For instance, Lejeune & Warnant (2008) provided a quantitative assessment of the influence of ionospheric irregularities on short-baseline Real Time Kinematics (RTK). An increase in the positioning errors during the St. Patrick's Day storm of dual-frequency (DF) based models such as Network-RTK (N-RTK) and Precise Point Positioning (PPP) was illustrated (e.g., Jacobsen & Andalsvik, 2016; Yang et al., 2020). More recently, Lu et al. (2020) evaluated the performance of Single Point Positioning (SPP) and PPP in Hong Kong during the same ionospheric storm. Follestad et al. (2021), in turn, investigated the quality of the Norwegian positioning service based on network RTK and its dependency on ionospheric irregularities.

*Corresponding author: jacek.paziewski@uwm.edu.pl

The researchers have attempted to handle the adverse impact of ionospheric disturbances on GNSS positioning (Hernández-Pajares et al., 2017). Respective research on this topic was conducted, for example, by Wanninger (2004), who proposed to use the I_{95} index that provides statistical information to support RTK and N-RTK, and by Park et al. (2017), who refined the stochastic model of RTK positioning and exploited Total Electron Content (TEC) maps. The feasibility of precise long-range positioning with an enhanced RTK model under the ionospheric disturbance was reported in Sieradzki & Paziewski (2016) and Paziewski & Sieradzki (2020). Additionally, Vadakke Veettil et al. (2020) refined the stochastic model of DF PPP to meet the challenges of GNSS positioning in the ionospheric scintillation environment. Another solution to enhance positioning performance under such unfavorable ionospheric conditions is to improve the signal tracking algorithms of the receiver (Susi et al., 2017; Xu et al., 2015). More recently, Monte-Moreno et al. (2021) proposed to support GNSS positioning with a forecasted Rate of TEC Index (ROTI) that may indicate ionospheric activity.

The ionospheric disturbances are more frequently observed and more challenging to handle at high latitudes (van der Meeren et al., 2014; Prikryl et al., 2015; Wang et al., 2016; Jin et al., 2018; Beeck & Jensen, 2021; Sieradzki & Paziewski, 2022). Recently, these areas have been subject to emerging human activity, including explorations and research expeditions that, e.g., for safety reasons, should be supported with reliable and precise navigation. Therefore, the performance of GNSS positioning in the Arctic is of high interest to the scientific community and commercial users. Relevant investigations on the correlation between the accuracy of PPP and the occurrence of ionospheric disturbances in such areas may be found in Jacobsen & Dähnn (2014), Juan et al. (2018), Fabbro et al. (2021). These studies were followed by Guo et al. (2021), who proposed and validated a novel method for mitigating the high latitude scintillation effects on PPP using the dataset collected in the Arctic and northern Canada during the geomagnetic storm in 2019.

However, no similar studies have been conducted for Greenland, which motivated us to assess the impact of ionospheric irregularities on GNSS positioning in this region. This study evaluates the performance of positioning methods that were not yet comprehensively investigated but are desired by a wide range of users. In this regard, we address (1) the needs of mass-market users that most frequently employ single-frequency (SF) receivers and expect a meter to submeter-level accuracy in an absolute mode, and (2) users who require the highest precision solution based on geodetic-grade DF receivers. For the former group, the ionospheric delay is considered the main contributor to the error budget (Orus Perez, 2017).

We have employed two techniques of GNSS positioning, namely PPP and RTK. The former is a stand-alone precise positioning technique. In normal conditions, PPP may achieve a positioning accuracy of decimeter- to centimeter-level conventionally using DF observations supported by precise satellite orbits and clocks products. As discussed before, the performance of DF-PPP under ionospheric disturbances has already been thoroughly validated. Therefore, we fill a gap and employ a single-frequency ionosphere-free (IF) PPP model (SF-IF PPP) based on a GRoup And PHase Ionospheric Correction (GRAPHIC) linear combination (LC) of phase and code observations (Yunck, 1996). The application of such a model is justified by a high demand for precise positioning among the users of mass-market SF receivers. Alternatively, an uncombined SF-PPP model may be used in such cases, as shown in Zhang et al. (2018), Zhao et al. (2021).

Relative positioning models, including RTK, provide the most accurate solution among all GNSS-based positioning approaches. The performance of integer ambiguity fixing in RTK is strongly related to the decorrelation of ionospheric delays. The decorrelation increases correspondingly to the baseline length. Enhanced models such as Network-RTK are, in turn, dependent on the accuracy of interpolated ionospheric corrections (Paziewski, 2016; Prochniewicz et al., 2017). In this case, simultaneous processing of the observations from neighboring reference stations allows the retrieval of information on ionospheric delay, which can be applied to support the rover solution (Prochniewicz et al., 2020). However, under the occurrence of ionospheric disturbances, such corrections are degraded (Wielgosz et al., 2005).

To provide a challenging scenario for determining the impact of the ionospheric irregularities on GNSS positioning in Greenland, we used datasets acquired under disturbed ionospheric conditions. The analysis and results specifically address the St. Patrick's Day storm on March 17, 2015, the storm of June 22, 2015, and the disturbing conditions in the period of August 25–26, 2018.

This paper is organized as follows. After describing the experiment design and dataset, we characterize ionospheric and space weather conditions during three selected periods of ionospheric irregularities. Then, we describe the employed observation and correction models of positioning and present the details of the processing strategy. Next, we show and discuss the results of GNSS positioning in Greenland, given the state of the ionosphere, and analyze cycle slip occurrence to understand the positioning results. Finally, we provide the conclusions in the last section.

2 Dataset

We use GNSS observations collected by selected permanent GNSS stations of Greenland GPS Network (GNET), an international project run by the Ohio State University, the National Space Institute at the Danish Technical University, and the University of Luxembourg. The observations acquired during three ionospheric storms were used:

1. St. Patrick's Day storm of March 17, 2015, Day-of-Year (DOY) 76/2015;
2. The storm of June 22, 2015, DOY 173/2015;
3. The storm of August 25–26, 2018, DOYs 237–238/2018.

We refer to the performance of positioning during the ionospherically disturbed periods as the benchmark results for the quiet periods, as follows:

- March 5 and 11, 2015, DOYs 64 and 70/2015, are the days of low and medium ionospheric activity, which

Table 1. The stations of the GNET network employed in GNSS positioning. We note that at the KMJP and MARG stations, the receivers were changed in 2018.

RINEX ID	Location	Latitude [°]	Longitude (West) [°]	Height [m]	Receiver type	Antenna type
KMJP	Kap Morris Jessup	83.643238	33.377086	85.2	Trimble NETRS/AlertGeo Resolute	TRM29659.00
YMER	Ymer Nunatak	77.432896	24.326329	1070.1	Trimble NETRS	TRM59800.00
MARG	Marie Gletscher	77.187039	65.694603	669.0	Trimble NETRS/AlertGeo Resolute	TRM29659.00
KBUG	Koge Bugt	65.143690	41.157545	289.4	Trimble NETRS	TRM29659.00
TREO	Trefoldighedens	64.277070	41.375079	121.9	Trimble NETRS	TRM29659.00
HJOR	Hjornefjeldet	63.418211	41.147870	762.7	Trimble NETRS	TRM29659.00
SENU	Sermip Nunataa	61.069581	47.141317	667.0	Trimble NETRS	TRM29659.00

constitute benchmarks for the positioning results obtained during the St. Patrick's Day storm;
- June 19, 2015, DOY 170/2018 serves as the benchmark for the positioning results obtained during the storm of June 2015;
- August 13–14, 2018, DOYs 225–226/2018 constitute benchmarks for the positioning results obtained during the storm of August 2018.

Table 1 provides the details of the GNSS stations used in the experiment, while Figure 1 shows their localization. The selection of the stations addresses the requirement of diverse distribution over Greenland. We use all the listed stations for absolute positioning with the PPP method. In the case of RTK, we take advantage of two representative baselines built between HJOR, TREO, and KBUG stations.

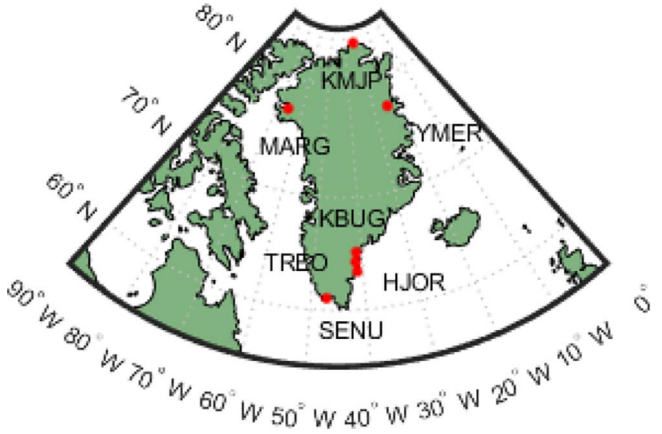

Figure 1. Distribution of GNSS permanent stations of the GNET network used in GNSS positioning.

3 Space weather and ionospheric conditions

3.1 Space weather conditions

The St. Patrick's Day solar magnetic storm (March 17, 2015) can be traced back to major coronal mass ejections (CMEs) at the Sun on March 15, 2015. The CMEs were accompanied by strong flares and radio bursts. The main phase of the storm consisted of two intervals of the southwardly oriented interplanetary magnetic field (IMF) (top panel of Fig. 2). Both had large southward components of IMF of values down to −20 nT, which propagated with an average speed of ~600 m/s. During the initial interval SYM-H index dipped to ~ −100 nT (~9:30 UT), whereas in the second case, the minimum was below ~230 nT (~23:00 UT). The latter, stronger and long-lasting phase, resulted in a large expansion of the auroral to ~60° and ~50° of the geomagnetic latitude on the dayside and nightside, respectively.

The characteristics of the geomagnetic storm of June 22, 2015, differed from these of the St. Patrick's Day storm. The interplanetary coronal mass ejection (ICME) hit the Advanced Composition Explorer (ACE) satellite at 18:00 UT with a step-like increase in solar wind density and velocity. At the same time, B_z and B_y of IMF turned negative for around one hour (middle panel of Fig. 2). The impact of solar wind magnetic pressure on the magnetosphere was strong for a shorter period. It led to a compression of the magnetosphere and strong auroral oval currents and scintillations. The effect was caused by two principal structures of ICMEs (sheaths and flux ropes) that drive major space weather storms (Kilpua et al., 2017). In the case of this storm, the minimum SYM-H index reached ~140 nT.

The events on August 25–26, 2018, were characterized by the impact of an ICME flux rope structure. At 12:00 UT, August 25, the ACE satellite observed the arrival of IMCE, which implicated a reorientation of IMF (bottom panel of Fig. 2). The B_z turned negative to about −10 nT and stayed negative for the next 24 h. At the same time, B_y is only negative over 9 h. The initial part of the event (until the end of August 25) was relatively weak and was classified as G1. The continuous southward orientation of IMF during the next day resulted in the intensification of the storm to the G3 level and enhanced auroral currents.

3.2 Analysis of ROTI and VTEC values at the GNSS permanent stations employed in the experiment

We precede the positioning assessment with the characterization of the ionospheric conditions over Greenland with GNSS-based ROTI and vertical TEC (VTEC). ROTI is defined as the standard deviation of the rate of change of slant TEC (STEC) over an adopted time interval of 5 min (Pi et al., 1997) to illustrate variations in ionospheric density (Monte-Moreno et al., 2021). STEC is computed using a geometry-free (GF) linear combination of undifferenced line-of-sight GPS L1 and L2 phase observations. The background ionization of the ionosphere is described by VTEC. VTEC time series at the Greenland GNSS stations were obtained through spatio-temporal interpolation,

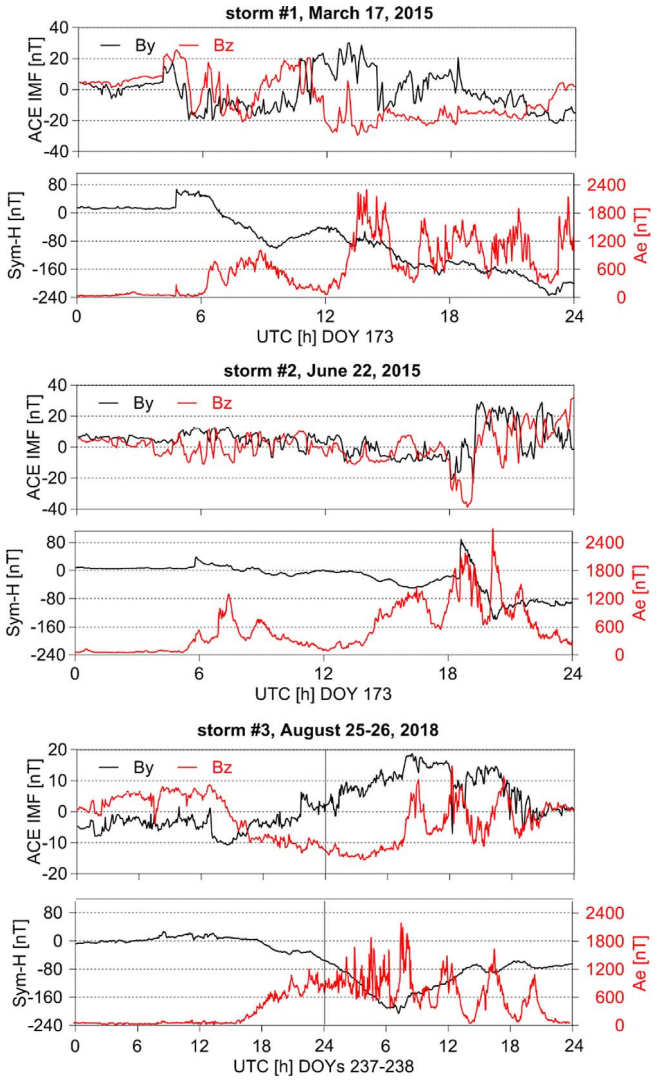

Figure 2. Stack plot of ACE observations and ground-based magnetic indices during the St. Patrick's Day storm on March 17, 2015 (top panel), the storm of June 22, 2015 (center panel), and the disturbed conditions on August 25–26, 2018 (bottom panel). Data source: NASA OMNIWeb.

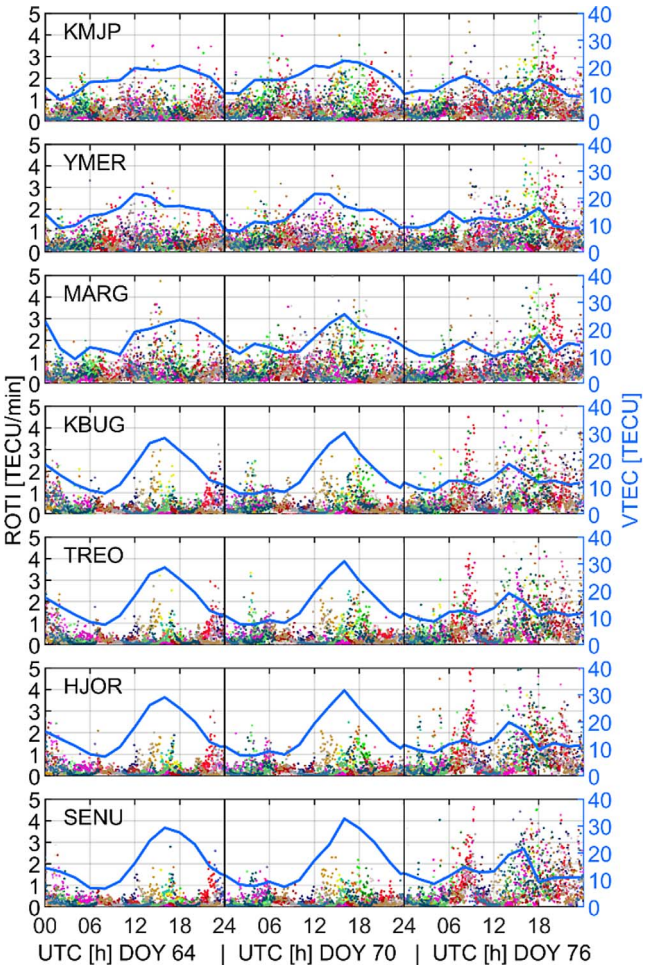

Figure 3. ROTI and VTEC time series at selected GNSS stations during the St. Patrick's Day storm of March 17, 2015 (DOY 76) and for the days of low (March 5, 2015, DOY 64) and medium (March 11, 2015, DOY 70) ionospheric activity. Colors distinguish the values for different GPS satellites.

using final International GNSS Service (IGS) global ionospheric maps provided in the IONEX files.[1]

Figures 3–5 present the ROTI time series computed using GPS observations acquired by the selected stations of the GNET network during the ionospheric storms and the days that precede the events. These results are overplotted with the time series of VTEC over the GNSS stations. The selected periods are indeed characterized by high dynamics of the ionospheric delay, which is mirrored in the ROTI values reaching incidentally even up to 4 TECU/min on March 17, 2015, and over 3 TECU/min during the next two ionospheric storms of June 22, 2015, and August 25–26, 2018, respectively. On the contrary, for the undisturbed period of August 13–14, 2018, ROTI values mostly do not exceed 0.2 TECU/min.

If we further investigate Figures 3–5, we find that ROTI values exhibit much higher values during the first storm than during the second one. Moreover, even March 5 and 11, 2015, although considered as the days of lower ionospheric activity compared to March 17, are subject to high ROTI fluctuations. These fluctuations are close to those for the disturbed days during the storms that occurred in June 2015 and August 2018, respectively.

What also follows from Figures 3 to 5 is that we may easily distinguish between two groups of the stations that exhibit a different nature of the ROTI time series, namely the stations located in the north (KMJP, MARG, and YMER) and those in the south of Greenland (KBUG, TREO, HJOR, SENU). That finding is especially evident for the ROTI time series during the storm of August 2018 since the southern stations exhibit several times higher ROTI than the northern ones and reach values even higher than those during the St. Patrick's Day storm. The reason for such strong amplification of ROTI during the main phase of the storm in 2018 is the occurrence of small and medium irregularities resulting from auroral precipitation and the position of the latter directly above the test network

[1] https://cddis.nasa.gov/archive/gnss/products/ionex/ (accessed 12.1. 2022)

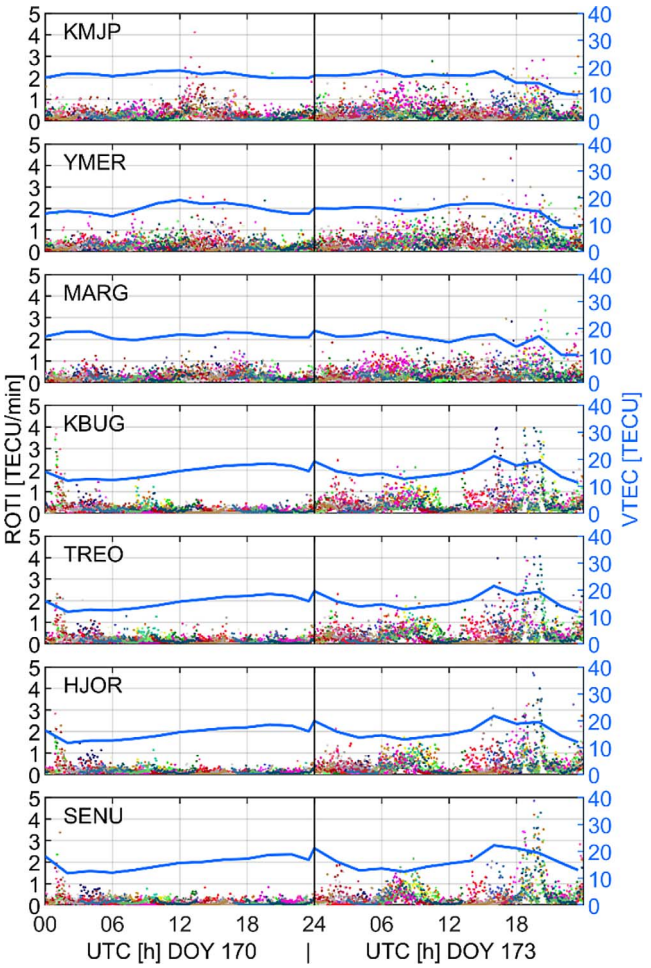

Figure 4. ROTI and VTEC time series at selected GNSS stations during the storm of June 22, 2015 (DOY 170) and for the undisturbed day (June 19, 2015, DOY 173). Colors distinguish the values for different GPS satellites.

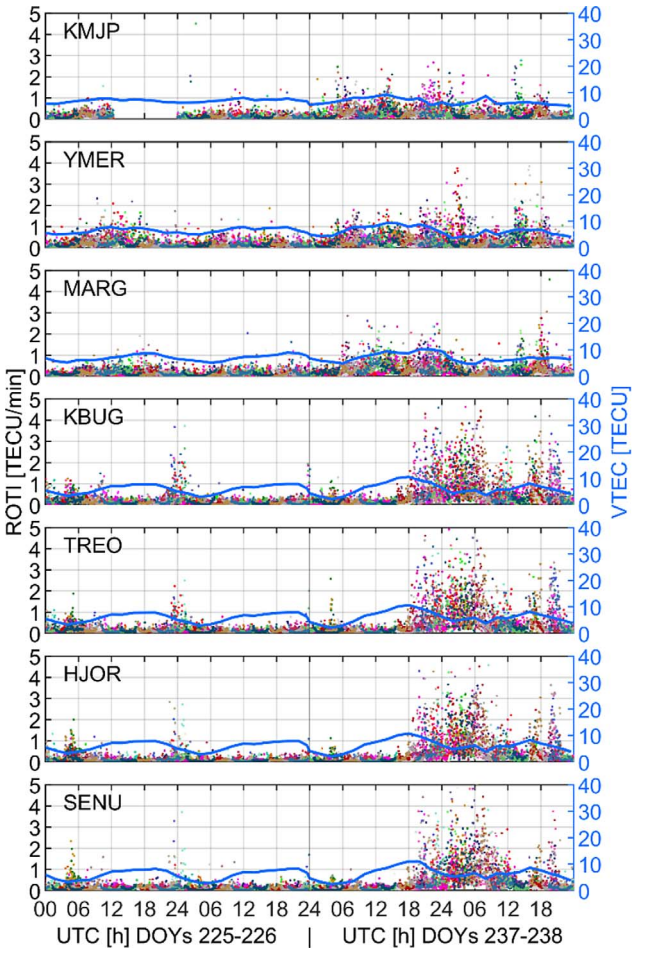

Figure 5. ROTI and VTEC time series at selected GNSS stations during the storm of August 25–26, 2018 (DOYs 237–238) and for the undisturbed days (August 13–14, 2015, DOYs 225–226). Colors distinguish the values for different GPS satellites.

(Paziewski & Sieradzki, 2020). The detailed analysis of ionospheric conditions in that study confirmed that the polar part of the ionosphere was relatively quiet in this case. It, in turn, explains the lack of strong TEC fluctuations for the northern stations.

As we may also read from Figures 3 to 5, the days in March 2015 are characterized by a larger ionospheric delay manifested in VTEC compared to the storms in June 2015 and August 2018. In the case of the storm in March 2015, we can observe an evident daily pattern of VTEC related to variations in the relative position of the solar terminator and selected networks. As expected, it is particularly pronounced for the stations located in southern Greenland, where the maximal VTEC reaches even 30 TECU. We also note that the St. Patrick's Day storm exhibits lower values of VTEC as compared to the undisturbed days that precede the event, namely March 5 and 11. This negative phase of the ionospheric storm that occurs only at high latitudes on the disturbing day of March 17, 2015, has been previously reported (Astafyeva et al., 2015). According to the multi-instrumental analysis, the possible reason for this depletion is the variation of the thermospheric composition. The VTEC time series for the storms of June 2015 and August 2018 do not reveal such significant daily changes, and their values do not exceed 20 TECU and 10 TECU, respectively. Such effects result from a modified position of the solar terminator that was shifted far beyond the pole during the storm of June 2015 and low solar activity during the one of August 2018.

4 Positioning models

This section details the employed functional, correction, and stochastic positioning models. The models are implemented in an in-house scientific GNSS software for data processing (Paziewski, 2015).

4.1 Single-Frequency Precise Point Positioning observation model

The model that meets the demands of users of mass-market SF receivers is based on the GRAPHIC linear combination of SF phase and code observations (Sterle et al., 2015;

Paziewski, 2022). This combination eliminates the ionospheric delay by making use of the fact that the ionospheric refraction causes the delay in code and phase observations, which are acquired on the same frequency, of the same magnitude but with the opposite sign.

Let us recall the observation equations of undifferenced phase and code GNSS signals as follows:

$$\begin{aligned} P^s_{r,j} &= \rho^s_r + c\cdot(\mathrm{d}t_r - \mathrm{d}t^s) + \mathrm{dTrop}^s_r + \mathrm{dIon}^s_{r,j} \\ &\quad + b_{r,j} - b^s_j + \epsilon^s_{r,P} \\ \Phi^s_{r,j} &= \rho^s_r + c\cdot(\mathrm{d}t_r - \mathrm{d}t^s) + \mathrm{dTrop}^s_r - \mathrm{dIon}^s_{r,j} \\ &\quad + \lambda_j\cdot N^s_{r,j} + B_{r,j} - B^s_j + \epsilon^s_{r,\Phi} \end{aligned} \tag{1}$$

where P and Φ refer to the code and phase observation in meters between the satellite s and the receiver r on frequency j, respectively; ρ stands for the geometric distance between the satellite and receiver; c is the speed of light in meters per seconds; $\mathrm{d}t_r$ denotes the receiver clock correction in seconds, while $\mathrm{d}t^s$ is the satellite clock correction in seconds; dIon and dTrop are the slant ionospheric and tropospheric delays in meters, respectively; λ refers to the signal wavelength in meters; N is the integer ambiguity of the phase observable in cycles; B_r and B^s are the receiver and satellite phase delays in meters, while b_r and b^s correspond to the receiver and satellite delays of code observations in meters, respectively; finally, ϵ is the observation noise coupled with the multipath effect.

Then, after forming a GRAPHIC linear combination of the observations given in (1) and applying satellite corrections, the functional model of SF-IF PPP can be written as:

$$\begin{aligned} 0.5\cdot\left(P^s_{r,j} + \Phi^s_{r,j}\right) &= \rho^s_r + c\cdot\mathrm{d}\bar{t}_r + mw^s_r\cdot\mathrm{ZWD}_r \\ &\quad + A^s_r + \epsilon^s_{r,SF-IF} \end{aligned} \tag{2}$$

where mw refers to the coefficient of the non-hydrostatic (wet) tropospheric mapping function; ZWD is the hydrostatic component of the zenith tropospheric delay; A is the non-integer phase ambiguity term that couples a half of the integer phase ambiguity and constant satellite biases. The temporally variable receiver hardware bias is modeled as a parameter coupled with the receiver clock offset ($\mathrm{d}\bar{t}_r$).

The vector of estimates comprises the corrections to the a priori geocentric coordinates, the receiver clock offset term, a non-hydrostatic tropospheric delay at the zenith direction, and a set of non-integer ambiguity parameters.

4.2 Real-Time Kinematics observation model

To account for the impact of the ionospheric delay in RTK positioning, we parametrize the double differenced (DD) slant ionospheric delays taking advantage of dual-frequency phase and code GNSS observations (Bock et al., 1986; Kashani et al., 2007; Paziewski, 2016). Due to insufficient densification of the GNSS permanent network in Greenland and thus infeasibility to generate precise ionospheric corrections, these are not used to support the rover solution. Such a model is called the ionosphere-float and is a special case of the ionosphere-weighted one (Odijk et al., 2012). The system of observation equation with DD DF phase and code signals between stations r, l and satellites s, n, here generalized to the frequency j, can be expressed as:

$$\begin{aligned} \Phi^{sn}_{rl,j} &= \rho^{sn}_{rl} + mw^s_r\mathrm{ZWD}_k - mw^n_r\mathrm{ZWD}_r - mw^s_l\mathrm{ZWD}_l \\ &\quad + mw^n_l\mathrm{ZWD}_l - \mu_j\mathrm{dIon}^{sn}_{rl} + \lambda_j N^{sn}_{rl,j} + \epsilon^{sn}_{rl,\Phi} \\ P^{sn}_{rl,j} &= \rho^{sn}_{rl} + mw^s_r\mathrm{ZWD}_r - mw^n_r\mathrm{ZWD}_r - mw^s_l\mathrm{ZWD}_l \\ &\quad + mw^n_l\mathrm{ZWD}_l + \mu_j\mathrm{dIon}^{sn}_{rl} + \epsilon^{sn}_{rl,P} \end{aligned} \tag{3}$$

in which μ represents the constant coefficient employed for converting the ionospheric delay on the first frequency into that on the selected one (j).

The corrections to a priori coordinates and zenith non-hydrostatic delays, a set of epoch-wise DD ionospheric delays, and a set of phase ambiguities are the unknown estimates in this model.

4.3 Correction and stochastic models

Conventional correction models were considered (Kouba, 2015), and products were used to support GNSS positioning (Dow et al., 2009). The details of the processing strategy and employed models are summarized in Table 2.

5 Impact of ionospheric irregularities on GNSS positioning in Greenland

In this section, we discuss the impact of ionospheric irregularities on the performance of GNSS positioning in Greenland. We investigate the quality of RTK and PPP in the coordinate domain. For RTK, we also evaluate the ambiguity resolution performance. We intentionally reinitialize the filter after every three hours to be able to investigate the convergence time (CT) and time-to-fix (TTF) for PPP and RTK techniques, respectively. Conventionally, we distinguish all the performance statistics by taking the ionospheric conditions as a criterion. Therefore, the results for ionospherically disturbed and undisturbed periods are given separately.

5.1 Implications for RTK performance

We analyze the positioning performance starting with the RTK technique that addresses the requirements of the most demanding users. We use the mean and standard deviation (STD) of coordinate errors as indicators of the performance of the RTK fixed solution. The former reflects the systematic errors present in the coordinates, whereas the latter is a measure of the coordinate dispersion. The float solution is characterized by the root mean square of three-dimensional coordinate error (3D-RMS). Coordinate errors are computed as differences between the benchmark and epoch-wise coordinates obtained in the kinematic solution.

Ambiguity Resolution Success Rate (ARSR) and Time-to-Fix (TTF) describe the ambiguity resolution performance. The former parameter illustrates the ratio of epochs with correctly fixed ambiguities to the number of all epochs. The latter indicator refers to the period required to achieve and keep a correctly

Table 2. Summary of the processing strategy and correction models depending on the adopted positioning model.

Parameter	PPP positioning	RTK positioning
Functional model	SF-IF PPP	ionosphere-float kinematic relative positioning
Observation	GRAPHIC LC of GPS carrier-phase and pseudorange	DF DD carrier-phase and pseudorange
Observable weighting scheme	An elevation-dependent scheme based on the cosecant function	
Zenith-referenced a priori sigma of observables	Pseudorange 30 cm; carrier-phase 3 mm	
Elevation cut-off angle	10°	
Sampling interval	30 s	
Satellite orbits and clock products	Precise final provided by IGS	
Receiver clock	Estimated as a white noise-like parameter	Eliminated due to double-differencing
Satellite code biases handling	Corrected with CODE products (Villiger et al., 2019)	
Tropospheric delay handling	A priori corrections from Saastamoinen's (Saastamoinen, 1973) model and GMF mapping function (Boehm et al., 2006); Wet Zenith Tropospheric Delays are estimated	
Ionospheric delay handling	Eliminated with GRAPHIC LC	DD ionospheric delays are estimated as loosely constrained parameters
Ambiguity handling	Estimated as float constants over each continuous observation arc	estimated and fixed to integers with MLAMBDA (Chang et al., 2005) and validated with W-ratio (Wang et al., 1998)
Parameter estimation method	Kalman filter	
Station coordinate handling	Static	Kinematic
Antenna phase center offsets and variations	Corrected with Antex igs14.atx (Rebischung et al., 2016)	
Relativistic effects, tides, phase wind-up effect	Corrected (Kouba, 2015; Wu et al., 1992)	

fixed position with 3D-RMS lower than the adopted threshold of 5 cm that is assuring a correct ambiguity fixing.

RTK positioning was performed in a single-baseline mode for two baselines of 96 km and 192 km (Fig. 6). In each case, the HJOR station serves as a fixed reference station, while TREO and KBUG are treated as the simulated user rover receivers. We note that such a long inter rover-reference station distance creates a challenging scenario for RTK positioning due to a high decorrelation of the atmospheric propagation errors.

Figures 7–9 illustrate RTK positioning error time series for the analyzed ionospheric storms, namely the St. Patrick's Day storm, the storm of June 22, 2015, and the storm of August 25–26, 2018, respectively. The grey color depicts the coordinate errors of the float solution, while green shows the results after the integer ambiguity fixing. The plots clearly show expected peaks in coordinate residuals of the float solution shortly after each three-hour session and the convergence to the accuracy level of 1–2 dm depending on the coordinate component and baseline. Since the filter was intentionally restarted every three hours, the presence of such peaks is fully justified. Nonetheless, after correct ambiguity fixing, the horizontal coordinate errors fall within the ±3 cm range.

More importantly, the coordinate errors given in Figures 7–9 suggest a decline in the accuracy of the RTK positioning, especially of the float solution, during the ionospherically disturbed periods. It is particularly evident in the positioning results for the weakest storm, which is the one of August 25–26, 2018, as presented in Figure 9. Less significant degradation of the positioning performance for the stronger events that occurred in March and June 2015 might be unexpected. It can still be explained by the position of the auroral oval related to the localization of the employed GNSS stations. According to the studies by Cherniak et al. (2015) and Cherniak & Zakharenkova (2017), both storms in 2015 are characterized by an extreme expansion of oval, up to 50° of geomagnetic latitude. Consequently, the strongest auroral disturbances are mainly observed below the southern boundary of Greenland, and thus, they do not affect the stations employed for RTK positioning to a great extent. In the case of the St. Patrick's Day storm, noticeable difficulties with ambiguity fixing occur only during the initial phase of the storm (~8.00 UTC, March 17, 2015) and after a short period of reorientation of IMF Bz (~15.00 UTC), as illustrated in Figure 7. Figure 8, in turn, reveals that the deterioration of RTK positioning is practically undetectable for the storm of June 2015. We attribute such effect to a very dynamic main phase of geomagnetic activity and, thus, a rapid equatorward expansion of the auroral oval.

A more comprehensive view of the RTK performance is provided in Table 3, where the statistics related to the ambiguity resolution domain are presented. The results confirm a noticeable impact of ionospheric disturbances on ambiguity resolution performance. In particular, we discover a clear drop of 13–16% in ambiguity resolution success rate during the St. Patrick's Day storm and a larger one reaching 27–37% during the storm of August 25–26, 2018 depending on the baseline, compared to the undisturbed days.

A deterioration of the ambiguity resolution performance that may be attributed to the ionospheric disturbances is also clearly reflected in the time required to achieve correct ambiguity fixing. Indeed, TTF was noticeably longer during the ionospherically disturbed periods than during the undisturbed ones. Taking as examples the results obtained during the St. Patrick's Day storm, we report that for the HJOR-KBUG baseline, a mean TTF was extended by 19.4 epochs up to

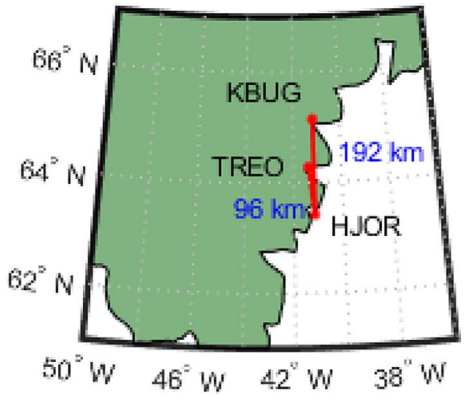

Figure 6. Baselines employed for RTK positioning.

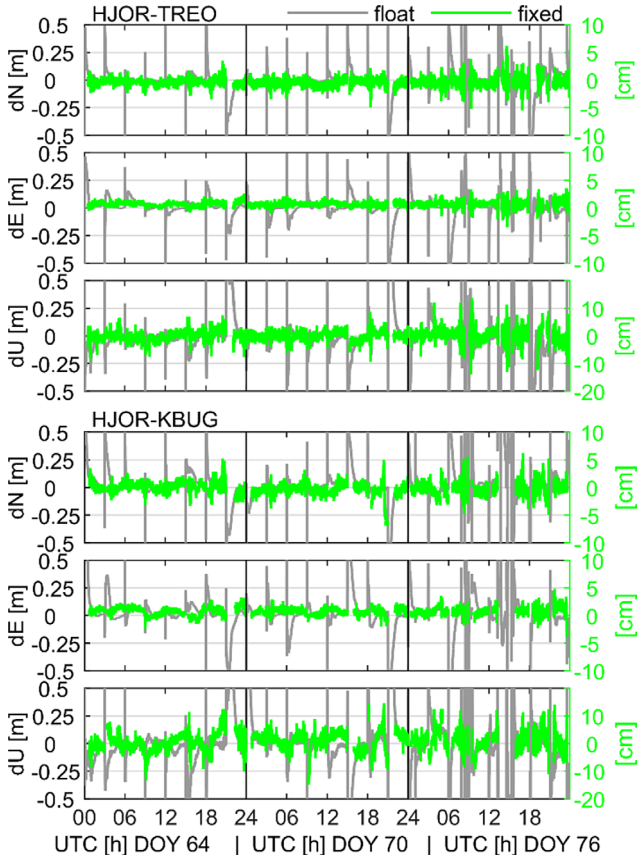

Figure 7. Time series of RTK float and fixed positioning errors of HJOR-TREO (three top panels) and HJOR-KBUG (three bottom panels) baselines during the St. Patrick's Day storm in 2015 (March 17, 2015, DOY 76) and for the undisturbed days preceding the event (March 5 and 11, DOYs 64, 70). One should note different *Y*-axis limits for the float and fixed solutions.

73.8 epochs, while for the HJOR-TREO baseline by 6.4 epochs up to 36.2 epochs. Such worsening in TTF driven by an occurrence of the ionospheric disturbances is even more pronounced for the storm in August 2018. In this case, mean TTF increased almost fourfold and fivefold for the HJOR-KBUG and

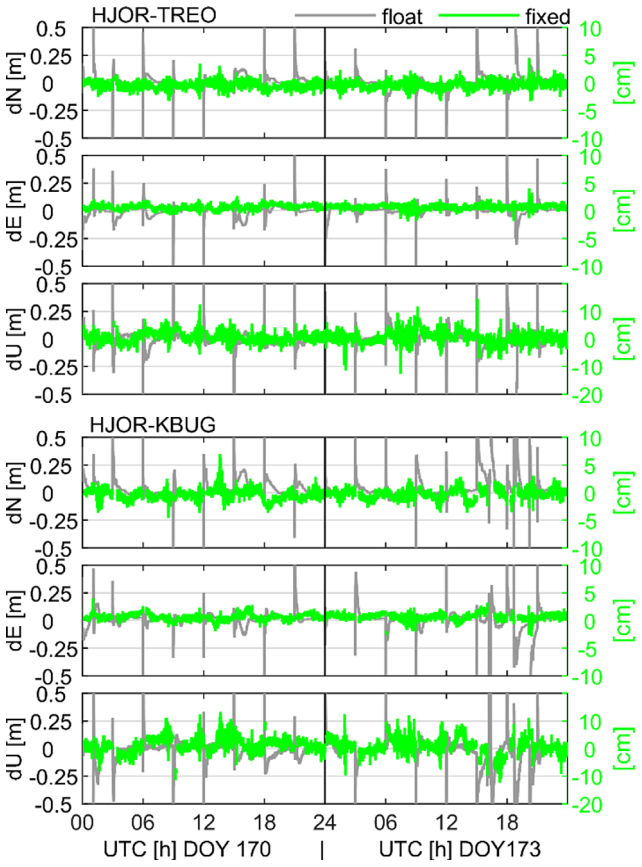

Figure 8. Time series of RTK float and fixed positioning errors of HJOR-TREO (three top panels) and HJOR-KBUG (three bottom panels) baselines during the storm of June 22, 2015 (DOY 173) and for the undisturbed day preceding the event (June 19, 2015, DOY 170). One should note different *Y*-axis limits for the float and fixed solutions.

HJOR-TREO baselines, respectively, after the emergence of the ionospheric irregularities (Table 3). A clear correlation between the presence of ionospheric disturbances manifested in ROTI, and an extension of the TTF is visualized in Figure 10, in which we show the RTK performance of the HJOR-KBUG baseline for the dataset of 2018.

After inspecting Table 3 again, we discover a significantly lower but still detectable adverse impact of ionospheric disturbances on ARSR for the HJOR-KBUG baseline of 192 km during the storm of June 22, 2015, compared to the results of the two other analyzed storms. For the shorter baseline of 96 km (HJOR-TREO), such an unfavorable effect of ionospheric irregularities is not revealed. However, considering the lengths of the baselines, we consider RTK positioning in June 2015 as having high performance, which is justified, e.g., by high ratios of ARSR reaching over ~96% and 86% for HJOR-TREO and HJOR-KBUG baselines, respectively. Overall, RTK's positioning during the event of June 2015 outperforms those of March 2015 and August 2018 in terms of ambiguity resolution performance. In particular, we experienced a higher ratio of epochs with correctly resolved ambiguities, and we required significantly less time to obtain correct ambiguity fixing.

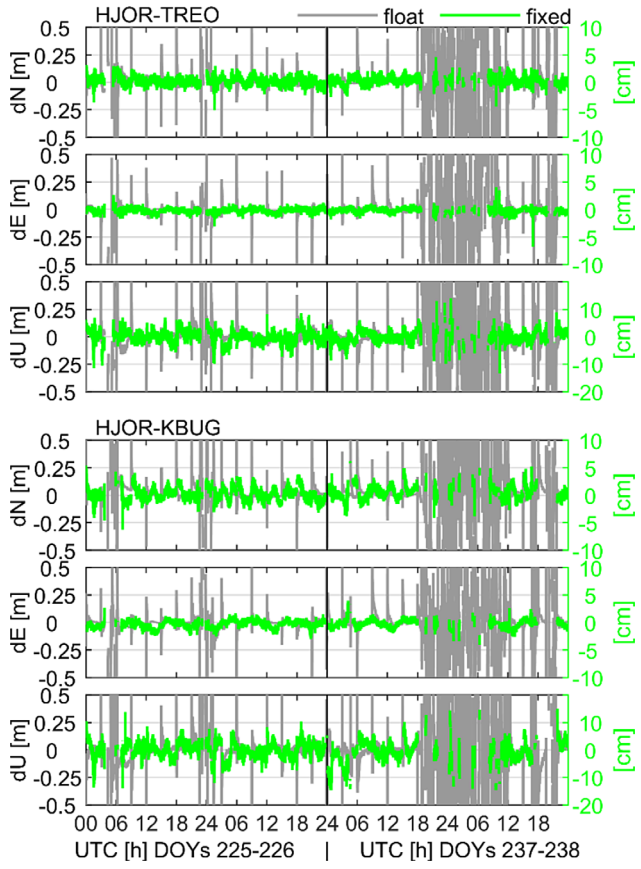

Figure 9. Time series of RTK float and fixed positioning errors of HJOR-TREO (three top panels) and HJOR-KBUG (three bottom panels) baselines during the storm of August 25–26, 2018 (DOYs 237–238) and for the undisturbed days preceding the event (August 13–14, 2018, DOYs 225–226). One should note different *Y*-axis limits for the float and fixed solutions.

Table 3 also reveals noticeable differences in RTK performance between the analyzed ionospheric storms reflected in the indicators describing the ambiguity resolution, namely ARSR and TTF. The main reason for that seems to be a unique spatio-temporal pattern of the ionospheric disturbances modulated to some extent by the phase of the solar cycle. We experienced the most vital deterioration of ambiguity resolution performance during the relatively weaker storm of August 2018. Thus, we consider small and medium auroral disturbances the most degrading factors. It is worth noticing that the storm of August 2018 corresponds to the period of low solar activity with small values of VTEC, as illustrated in Figure 5. This, in turn, also allows us to assume that the gradient of background ionization between the stations is an insignificant factor having no impact on RTK positioning.

The RTK performance confirms the finding on the substantial impact of auroral irregularities during two severe storms in 2015, which, as we recall, exhibit the strongest auroral disturbances below the southern boundary of Greenland. The ambiguity resolution performance during these storms is not worsened to a great extent. We observe a lower degradation of ARSR and TTF for the storm of March 2015 compared to that of August 2018 and practically no degradation for the storm of June 2015.

Nevertheless, the ARSR and TTF statistics for March and June 2015 differ significantly from each other, even for the quiet days. We believe that the more deteriorated results in March 2015 are at least partly driven by a different ionization level on the dayside (up to 30 TECU) and nightside (even below 10 TECU) hemispheres. Its natural consequence is an amplification of the ionospheric gradient between the stations and, thus, a growth of DD ionospheric delay. Furthermore, such a scenario induces an anti-sunward flow of polar patches providing additional distortion of the ionosphere.

Figure 11 characterizes the positioning performance in the coordinate domain for the float RTK solution. In this case, the residual part of DD ionospheric delays propagate to the other parameters of the model, including the coordinates. Consequently, we discover a substantial decline in the accuracy of the float solution manifested in at least twofold higher RMS of coordinate errors during the disturbed periods compared to the undisturbed ones for both the St. Patrick's Day storm and the storm of August 2018. This drop in the performance of the float solution is, again, significantly lower but still evident for the dataset of June 2015. We recall that high accuracy a priori coordinates are prerequisites for correct and fast ambiguity fixing in RTK. Therefore, the float solution of poor accuracy substantially affects the ambiguity resolution performance, as justified by the statistics in Table 3.

We examine cycle slips of phase observations to better understand poorer RTK performance during the ionospherically disturbed periods. The cycle slips detection is made using a temporal difference of DF geometry-free LC with a threshold of 0.7 m (Sieradzki & Paziewski, 2022). Such a limit is justified by the requirement of separating the cycle slips from the rapid changes of TEC induced by variations of the high-latitude ionosphere. Nonetheless, we note that the cycle slips below the applied threshold were extremely rare. A combined number of cycle slips for both L1 & L2 frequency bands is presented in Figure 12. The figure reveals that the increases in the number of cycle slips perfectly coincide with the declines in RTK positioning performance shown in Figures 7–9. In particular, one can see a spectacular increase in the number of cycle slips for the disturbed days of March 2015 and August 2018, illustrated in the top and bottom panels of Figure 12, respectively. This effect correlates well with a southward orientation of IMF B_z and the periods of intense particle precipitation (Fig. 2). It also confirms a strong dependency of GNSS phase observation quality on the occurrence of ionospheric irregularities. Such a large number of cycle slips adversely affects the accuracy of the float solution, as illustrated in Figure 11, and ambiguity resolution performance, as reported in Table 3 and visualized in Figure 10. During the storm of June 2015, the phase observations were affected by the cycle slips to a minor extent. Thus, the impact of this storm on RTK positioning performance is weaker, which is evidently reflected in the TTF, ASR, and 3D RMS of coordinate errors for the float solution. Further investigations based on temporal differences of the observations performed separately for L1 and L2 signals confirm that over 98% of the detected cycle slips affected the observations on the L2 frequency band. This outperformance of L1 in terms of susceptibility to CS is most likely related to its higher carrier-to-noise density ratio compared to the signals transmitted on L2 (Garner et al., 2011; Sato et al., 2019).

Table 3. Statistics of the integer ambiguity resolution performance in RTK positioning. We distinguish the statistics by taking the state of the ionosphere as a criterion. Undisturbed periods correspond to the quiet days treated as benchmarks.

Baseline	Ionospheric period	The St. Patrick's Day storm of March 17, 2015		The storm of June 22, 2015		The storm of August 25–26, 2018	
		ARSR [%]	Mean TTF [epochs]	ARSR [%]	Mean TTF [epochs]	ARSR [%]	Mean TTF [epochs]
HJOR-TREO	Undisturbed	91.5	29.8	95.7	16.1	96.2	9.3
	Disturbed	78.3	36.2	97.4	7.8	68.8	46.8
HJOR-KBUG	Undisturbed	84.0	54.4	90.9	29.1	87.8	26.9
	Disturbed	68.6	73.8	86.6	29.1	50.0	106.6

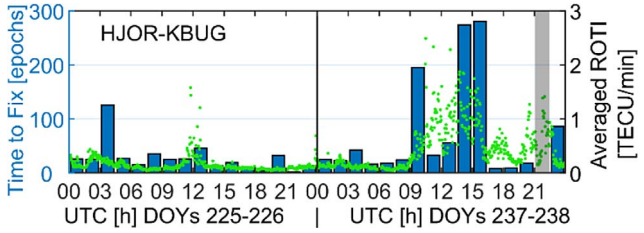

Figure 10. TTF for RTK positioning of HJOR-KBUG baseline during the disturbed conditions in the period of August 25–26, 2018, and two undisturbed days before the event. A grey bar corresponds to the session during which we did not achieve a correct ambiguity fixing within a time limit of 3 h. The ROTI values for the KBUG station given in green are averaged over all satellites.

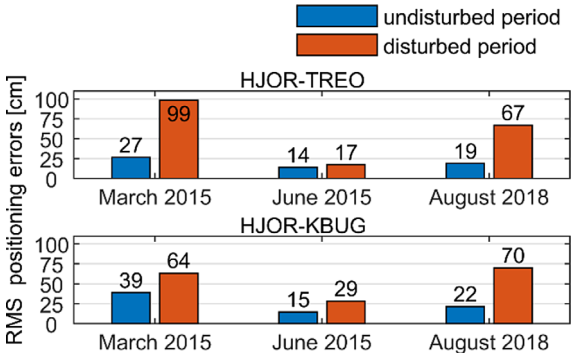

Figure 11. RMS of 3D positioning errors of float RTK solution during the analyzed ionospheric storms for HJOR-TREO and HJOR-KBUG baselines in the top and bottom panels, respectively. The statistics are distinguished, taking as a criterion the state of the ionosphere.

The mean coordinate biases and STDs for RTK with correctly fixed ambiguities are shown in Figure 13. As seen from the figure, fixed solution accuracy is high for disturbed and undisturbed periods. Specifically, the mean coordinate biases did not exceed 13 mm for any component. Depending on the baseline, coordinate STDs fitted the range of 4–13 mm and 18–38 mm for horizontal and vertical components, respectively. Nonetheless, a careful reader may discover that the presence of the ionospheric disturbances is correlated with a slight gain in STD and mean error of the height component. For example, the height STD of the HJOR-TREO baseline increased by 10 mm during the St. Patrick's Day storm on March 17, 2015, which is about half compared to the undisturbed days of March 5 and 11.

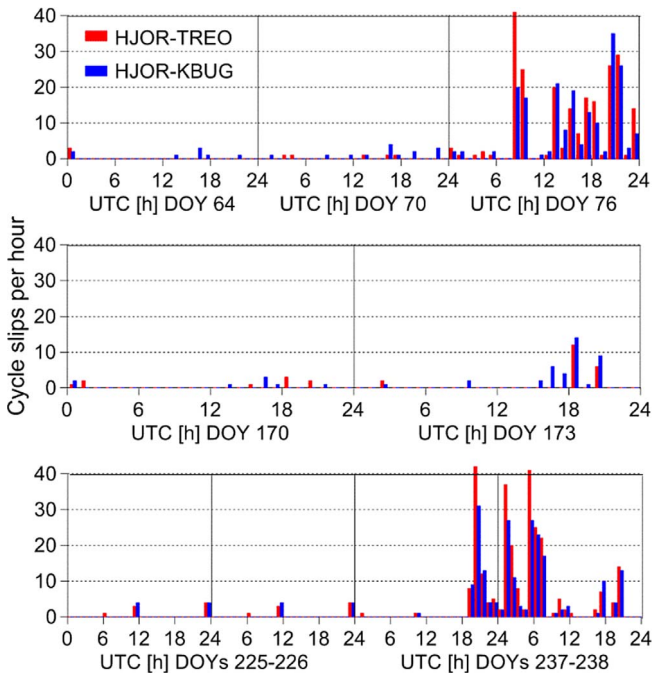

Figure 12. The total number of L1&L2 cycle slips per hour for HJOR-TREO and HJOR-KBUG baselines during the St. Patrick's Day storm on March 17, 2015 (top panel), the storm of June 22, 2015 (center panel), the disturbed conditions in the period of August 25–26, 2018 (bottom panel), and for the undisturbed days preceding the events.

The time series of positioning errors given in Figures 7–9 suggested that the accuracy of the fixed solution is higher for the shorter baseline, i.e., HJOR-TREO, compared to that of the HJOR-KBUG one. Indeed, this finding is also confirmed by the coordinate STDs presented in Figure 13. This effect could be expected if we recall that the former baseline is about two times shorter than the latter. Thus, remaining unmodelled atmospheric propagation errors are significantly lower. The outperformance of the HJOR-TREO baseline is also expressed in the TTF of subsequent three-hour-long sessions, as illustrated in Figure 10.

5.2 Implications for SF-IF PPP performance

We use 3D RMS of coordinate errors as the indicator of the positioning accuracy for the SF-IF PPP model. Conventionally, coordinate errors are obtained as differences between the SF-IF

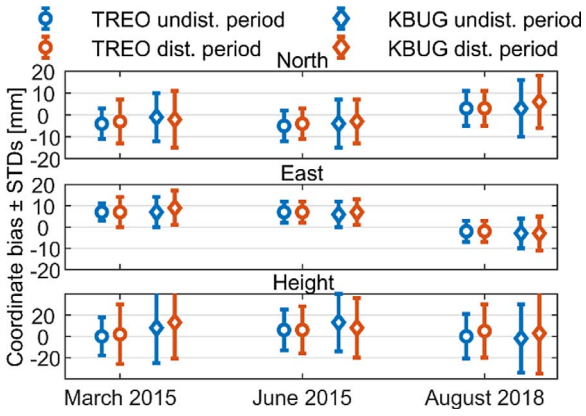

Figure 13. Coordinate statistics of RTK fixed solutions for HJOR-TREO and HJOR-KBUG baselines during analyzed events. The results are distinguished by adopting the ionosphere state as a criterion.

PPP coordinate estimates and the benchmark coordinates provided by IGS. An essential indicator of the PPP performance is the convergence time (CT) that characterizes how fast the position estimates converge to the specified accuracy level. We define CT as the period required to achieve and keep for at least 5 min a position with a 3D-RMS error lower than 0.5 m (Paziewski, 2022). The statistics obtained for each three-hour-long session were averaged over the whole dataset.

Figure 14 presents an example time series of SF-IF PPP positioning errors during the St. Patrick's Day storm for two representative stations, KMJP and SENU, located in northern and southern Greenland, as they are typical for all stations. The figures show how the filter converges rapidly after reinitialization induced intentionally every three hours. More importantly, the SF-IF PPP positioning error time series seem to be unaffected by any trends attributed to the magnitude of the ionospheric delay or its rapid changes reflected in ROTI. This finding is contrary to the results of RTK given in the previous section or past studies on PPP that, albeit, were based on dual-frequency solutions (Jacobsen & Andalsvik, 2016; Marques et al., 2018; Fabbro et al., 2021).

Figure 15 reports the 3D RMS of positioning errors for SF-IF PPP. We conventionally distinguish the statistics by adopting the presence of ionospheric disturbances as a criterion. After the filter's convergence, the SF-IF PPP reaches a comparable positioning accuracy for all periods and events characterized by 3D RMS fitting the range of 2–5 dm, depending on the station. Such a level of accuracy is expected and agrees with the previous studies (Bahadur & Nohutcu, 2021; Paziewski, 2022).

As shown in Figure 16, the SF-IF PPP filter requires about 20–47 min to reach the accuracy level defined with a 3D RMS error of 0.5 m. The analyses of the statistics given in Figure 16 do not allow us to firmly conclude the existence of a coincidence between the occurrence of the ionospheric disturbances and the extension in the convergence time. For several stations, the CT was longer during the ionospherically disturbed period. However, there were the stations such as YMER and HJOR during the St. Patrick's storm or MARG and SENU during the subsequent two events, for which the situation was the opposite. In the case of the storm of 2018, at large, we did not detect the deterioration of the convergence time during

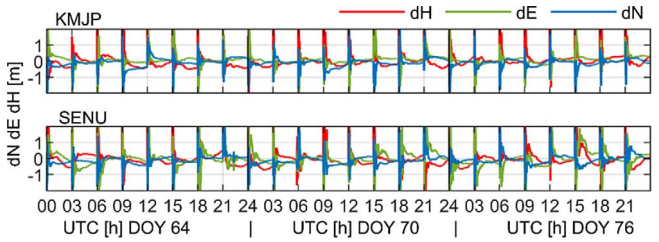

Figure 14. Time series of positioning errors of SF-SPP at KMJP and SENU stations in the top and bottom panels, respectively, during the St. Patrick's Day storm in 2015 (DOY 76) and for the undisturbed days that precede the event (DOYs 64 and 70).

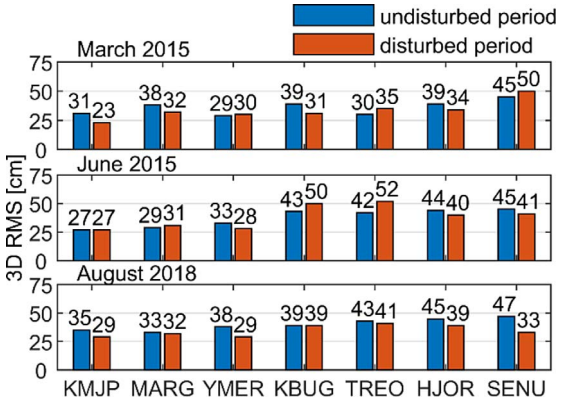

Figure 15. RMS of 3D positioning errors for SF-IF-PPP during the storms of March, and June 2015, the disturbing conditions in August 2018, and the undisturbed days that precede the events. The results are distinguished by adopting the ionosphere state as a criterion.

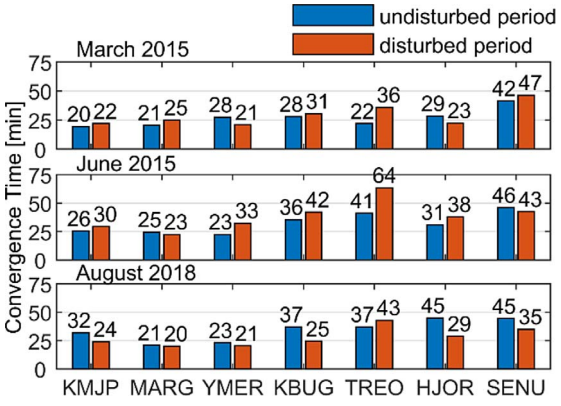

Figure 16. Convergence time of SF-IF-PPP during the storms of March, and June 2015, the disturbing conditions in August 2018, and the undisturbed days that precede the events. The results are distinguished by adopting the ionosphere state as a criterion.

the ionospherically disturbed period of August 25–26, 2018. SF-PPP is generally resistant to ionospheric disturbances as no apparent impact on positioning performance was revealed.

Even though the GRAPHIC linear combination is free from the impact of ionospheric delay, it may still suffer from the presence of cycle slips induced by ionospheric irregularities.

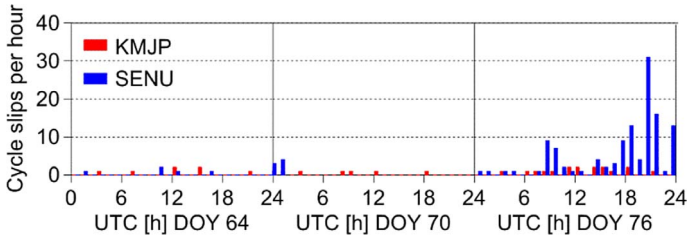

Figure 17. The total number of L1&L2 cycle slips of phase observations per hour during the St. Patrick's Day storm on March 17, 2015, and for the undisturbed days which precede the events at stations KMJP and SENU.

Thus, motivated by the RTK results, we also assess the quality of carrier-phase observations in this regard for the stations used for SF-IF PPP. The example results for the north (KMJP) and the south (SENU) stations during the St. Patrick's Day storm are presented in Figure 17.

By comparing the results for KMJP and SENU, it is evident that there are significant differences in the number of cycle slips between the stations. This is reasoned by a substantial meridional distance between KMJP and SENU stations, characterized by the corresponding geomagnetic latitudes of ~84° and ~65°, respectively. As a result, the observations of KMJP are not affected by auroral precipitation and do not suffer from any noticeable impact of the ionospheric storm. The opposite situation occurs for SENU, which latitude coincides with the storm-induced auroral oval. Consequently, on March 17, 2015, phase observations exhibited a significant increase in the number of cycle slips, even up to 30 per hour, which manifests a strong decline in the phase measurement quality.

Fortunately, we discovered that practically all cycle slips occur only at the L2 frequency band. It explains no evident impact of the ionospheric irregularities on SF-IF PPP performance. Such lack of susceptibility of L1 observations to cycle slips is an advantage of the positioning models based on single-frequency ionosphere-free LCs, such as SF-IF PPP. This property, in turn, predestines them for application to positioning under strong ionospheric disturbances.

Considering the properties of the GRAPHIC linear combination, a lack of cycle slips on the L1 frequency band, and finally, the obtained positioning results, we can exclude the impact of the ionosphere as a primary factor that drives the performance of SF-IF PPP. Nevertheless, analyzing further the statistics given in Figure 16, we can see noticeable differences between the stations' convergence time, which are worthy of investigation. We believe that such discrepancies are related to the other site-specific unmodelled effects. One possible explanation is the influence of coupled noise and multipath effects, which depend on the receiver and the surrounding environment. To verify this hypothesis, we analyze the quality check products routinely generated by UNAVCO.[2] In particular, we use the mean RMS of the MP1 multipath combination (Estey & Meertens, 1999), which can serve as an indicator of pseudorange uncertainty. Comparing MP1 statistics presented in Figure 18 with those of the convergence time shown in Figure 16, we notice a good agreement suggesting that code noise and multipath effect are important factors driving SF-IF PPP performance. In particular, we found larger CT and MP1 RMS values for the southern stations, such as SENU and TREO, whereas the lower ones for the northern stations (KMJP, MARG).

[2] ftp://data-out.unavco.org (accessed 12.1.2022).

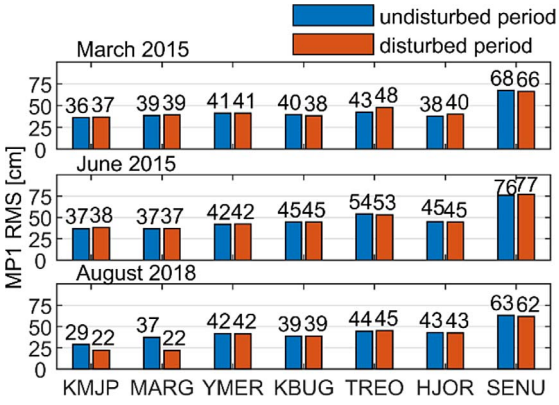

Figure 18. RMSs of MP1 linear combination for the stations employed in SF-IF-PPP performance assessment during the storms of March, June 2015, and August 2018.

Figure 18 also reveals that the MP1 RMS values are overall constant regardless of the ionospheric conditions, as expected. Noticeable changes in the MP1 are seen only for KMJP and MARG stations for the dataset of August 2018. However, such effects were caused by receiver changes at these stations, which, in turn, reduced the code observation noise.

6 Conclusions

This study addressed a research problem regarding the impact of ionospheric irregularities on GNSS positioning in Greenland. First, we briefly characterized Greenland's space weather and ionospheric conditions during three selected ionospheric storms of March 17, 2015, June 22, 2015, and August 25–26, 2018. We showed that the stations located in northern and southern Greenland exhibit different ionospheric conditions reflected in the nature of the ROTI and VTEC time series.

Then, we evaluated RTK positioning performance, which resulted in the following findings:

- We confirmed a significant impact of the ionospheric disturbances on the integer ambiguity fixing performance. Taking the storm of August 25–26, 2018, as an example, we discovered a clear drop in the ambiguity resolution success rate of about 27–37%, depending on the baseline,

under the presence of ionospheric disturbances. The evident extension of time-to-fix during that event was also revealed as the mean TTF increased fivefold for the HJOR-TREO baseline after the emergence of ionospheric anomalies.

- Further investigations revealed significant deterioration of the accuracy of float RTK positioning during the disturbed ionosphere periods. Considering the accurate a priori position provided by the float RTK solution as the prerequisite of successful ambiguity fixing, we can find the worsening in the ambiguity resolution domain as fully justified. We also showed a minor but noticeable impact of the ionospheric disturbances on fixed RTK accuracy, providing that the ambiguities were correctly resolved.
- The RTK positioning for the storm of June 2015 outperforms those for the storms of March 2015 and August 2018. In particular, we experienced higher ambiguity resolution success rates, and we required significantly less time to obtain correct ambiguity fixing. Such outcomes seem to be the consequences of less challenging ionospheric conditions during that event, i.e., weaker ionospheric disturbances reflected in ROTI and lower ionospheric delays expressed by TEC.

Assessing the SF-IF PPP positioning performance, it was demonstrated that the model was unaffected by the ionospheric disturbances as no apparent impact on the convergence time or positioning accuracy was detected. This finding is reasoned by a low susceptibility of L1 phase observations to the cycle slips generated by ionospheric irregularities. Therefore, the model based on the GRAPHIC linear combination is predestined for the application by the users of single-frequency, low-cost receivers in the areas of frequent ionospheric disturbances. Any differences among the GNSS stations in SF-IF PPP performance were driven by code observation noise and the multipath effect.

Finally, based on the observation analyses, we proved that phase signals on the L2 frequency band are more prone to cycle slips induced by ionospheric irregularities than those transmitted on the L1. This finding explains a noticeable decline in the DF RTK performance during the ionospherically disturbed period and a lack of such effect for the SF-IF PPP model.

Acknowledgements. This work is funded by ESA ITT "Forecasting Space Weather Impacts on Navigation Systems in the Arctic (Greenland Area)" Expro+, Activity No. 1000026374. The GNET GNSS observations from Greenland were kindly provided by the Danish Agency for Data Supply and Efficiency in the Danish Ministry of Energy, Utilities and Climate, Copenhagen, Denmark. The authors also acknowledge the availability of different products and observations from NASA/GSFC's Space Physics Data Facility's OMNIWeb service and OMNI data, CDDIS and UNAVCO. The editor thanks P.T. Jayachandran and Baocheng Zhang for their assistance in evaluating this paper.

References

Andalsvik YL, Jacobsen KS. 2014. Observed high-latitude GNSS disturbances during a less-than-minor geomagnetic storm. *Radio Sci* **49**: 1277–1288. https://doi.org/10.1002/2014RS005418.

Astafyeva E, Zakharenkova I, Förster M. 2015. Ionospheric response to the 2015 St. Patrick's Day storm: A global multi-instrumental overview. *J Geophys Res Space Phys* **120**: 9023–9037. https://doi.org/10.1002/2015JA021629.

Bahadur B, Nohutcu M. 2021. Real-time single-frequency multi-GNSS positioning with ultra-rapid products. *Meas Sci Technol* **32**: 014003. https://doi.org/10.1088/1361-6501/abab22.

Beeck SS, Jensen ABO. 2021. ROTI maps of Greenland using kriging. *J Geod Sci* **11**: 83–94. https://doi.org/10.1515/jogs-2020-0123.

Bock Y, Gourevitch SA, Counselman I, Charles C, King RW, Abbot RI. 1986. Interferometric analysis of GPS phase observations. *Manuscripta Geodaetica* **11**: 282–288.

Boehm J, Niell A, Tregoning P, Schuh H. 2006. Global Mapping Function (GMF): A new empirical mapping function based on numerical weather model data. *Geophys Res Lett* **33**: L07304. https://doi.org/10.1029/2005GL025546.

Chang X-W, Yang X, Zhou T. 2005. MLAMBDA: a modified LAMBDA method for integer least-squares estimation. *J Geod* **79**: 552–565. https://doi.org/10.1007/s00190-005-0004-x.

Cherniak I, Zakharenkova I. 2017. New advantages of the combined GPS and GLONASS observations for high-latitude ionospheric irregularities monitoring: case study of June 2015 geomagnetic storm. *Earth Planets Space* **69**: 66. https://doi.org/10.1186/s40623-017-0652-0.

Cherniak I, Zakharenkova I, Redmon RJ. 2015. Dynamics of the high-latitude ionospheric irregularities during the 17 March 2015 St. Patrick's Day storm: Ground-based GPS measurements. *Space Weather* **13**: 585–597. https://doi.org/10.1002/2015SW001237.

Dow JM, Neilan RE, Rizos C. 2009. The International GNSS Service in a changing landscape of Global Navigation Satellite Systems. *J Geod* **83**: 191–198. https://doi.org/10.1007/s00190-008-0300-3.

Estey LH, Meertens CM. 1999. TEQC: The multi-purpose toolkit for GPS/GLONASS data. *GPS Solut* **3**: 42–49. https://doi.org/10.1007/PL00012778.

Fabbro V, Jacobsen KS, Andalsvik YL, Rougerie S. 2021. GNSS positioning error forecasting in the Arctic: ROTI and Precise Point Positioning error forecasting from solar wind measurements. *J Space Weather Space Clim* **11**: 43. https://doi.org/10.1051/swsc/2021024.

Follestad AF, Clausen LBN, Moen JI, Jacobsen KS. 2021. Latitudinal, diurnal, and seasonal variations in the accuracy of an RTK positioning system and its relationship with ionospheric irregularities. *Space Weather* **19**: e2020SW002625. https://doi.org/10.1029/2020SW002625.

Garner TW, Harris RB, York JA, Herbster CS, Minter CF, Hampton DL. 2011. An auroral scintillation observation using precise, collocated GPS receivers: GPS observation of auroral scintillation. *Radio Sci* **46**: RS1018. https://doi.org/10.1029/2010RS004412.

Guo K, Vadakke Veettil S, Weaver BJ, Aquino M. 2021. Mitigating high latitude ionospheric scintillation effects on GNSS Precise Point Positioning exploiting 1-s scintillation indices. *J Geod* **95**: 30. https://doi.org/10.1007/s00190-021-01475-y.

Hernandez-Pajares M, Miguel Juan J, Sanz J, Aragon-Angel A, Garcia-Rigo A, Salazar D, Escudero M. 2011. The ionosphere: effects, GPS modeling and the benefits for space geodetic techniques. *J Geod* **85**: 887–907. https://doi.org/10.1007/s00190-011-0508-5.

Hernández-Pajares M, Wielgosz P, Paziewski J, Krypiak-Gregorczyk A, Krukowska M, Stepniak K, Kaplon J, Hadas T, Sosnica K, Bosy J, Orus-Perez R, Monte-Moreno E, Yang H, Garcia-Rigo A, Olivares-Pulido G. 2017. Direct MSTID mitigation in precise GPS processing. *Radio Sci* **52**: 321–337. https://doi.org/10.1002/2016RS006159.

Jacobsen KS, Andalsvik YL. 2016. Overview of the 2015 St. Patrick's day storm and its consequences for RTK and PPP positioning in Norway. *J Space Weather Space Clim* **6**: A9. https://doi.org/10.1051/swsc/2016004.

Jacobsen KS, Dähnn M. 2014. Statistics of ionospheric disturbances and their correlation with GNSS positioning errors at high latitudes. *J Space Weather Space Clim* **4**: A27. https://doi.org/10.1051/swsc/2014024.

Ji S, Chen W, Weng D, Wang Z, Ding X. 2013. A study on cycle slip detection and correction in case of ionospheric scintillation. *Adv Space Res* **51**: 742–753. https://doi.org/10.1016/j.asr.2012.10.012.

Jin Y, Miloch WJ, Moen JI, Clausen LBN. 2018. Solar cycle and seasonal variations of the GPS phase scintillation at high latitudes. *J Space Weather Space Clim* **8**: A48. https://doi.org/10.1051/swsc/2018034.

Juan JM, Sanz J, González-Casado G, Rovira-Garcia A, Camps A, Riba J, Barbosa J, Blanch E, Altadill D, Orus R. 2018. Feasibility of precise navigation in high and low latitude regions under scintillation conditions. *J Space Weather Space Clim* **8**: A05. https://doi.org/10.1051/swsc/2017047.

Kashani I, Wielgosz P, Grejner-Brzezinska D. 2007. The impact of the ionospheric correction latency on long-baseline instantaneous kinematic GPS positioning. *Surv Rev* **39**: 238–251. https://doi.org/10.1179/175227007X197156.

Kilpua E, Koskinen HEJ, Pulkkinen TI. 2017. Coronal mass ejections and their sheath regions in interplanetary space. *Living Rev Sol Phys* **14**: 5. https://doi.org/10.1007/s41116-017-0009-6.

Kouba J. 2015. A guide to using International GNSS Service (IGS) products. https://kb.igs.org/hc/en-us/articles/201271873-A-Guide-to-Using-the-IGS-Products.

Lejeune S, Warnant R. 2008. A novel method for the quantitative assessment of the ionosphere effect on high accuracy GNSS applications, which require ambiguity resolution. *J Atmos Sol Terr Phys* **70**: 889–900. https://doi.org/10.1016/j.jastp.2007.01.009.

Lu Y, Wang Z, Ji S, Chen W. 2020. Assessing the positioning performance under the effects of strong ionospheric anomalies with multi-GNSS in Hong Kong. *Radio Sci* **55**: https://doi.org/10.1029/2019RS007004.

Marques HA, Marques HAS, Aquino M, Veettil SV, Monico JFG. 2018. Accuracy assessment of precise point positioning with multi-constellation GNSS data under ionospheric scintillation effects. *J Space Weather Space Clim* **8**: A15. https://doi.org/10.1051/swsc/2017043.

Monte-Moreno E, Hernandez-Pajares M, Yang H, Rigo AG, Jin Y, Hoeg P, Miloch WJ, Wielgosz P, Jarmolowski W, Paziewski J, Milanowska B, Hoque M, Perez RO. 2021. Method for forecasting ionospheric electron content fluctuations based on the optical flow algorithm. *IEEE Trans Geosci Remote Sensing* **60**: 1. https://doi.org/10.1109/TGRS.2021.3126888.

Muhammad B, Alberti V, Marassi A, Cianca E, Messerotti M. 2015. Performance assessment of GPS receivers during the September 24, 2011 solar radio burst event. *J Space Weather Space Clim* **5**: A32. https://doi.org/10.1051/swsc/2015034.

Odijk D, Verhagen S, Teunissen PJG. 2012. Medium-distance GPS ambiguity resolution with controlled failure rate. In: *Geodesy for Planet Earth, International Association of Geodesy Symposia*. Kenyon S, Pacino MC, Marti U, (Eds.) Springer, Berlin Heidelberg, Berlin, Heidelberg. pp. 745–751. https://doi.org/10.1007/978-3-642-20338-1_93.

Orus Perez R. 2017. Ionospheric error contribution to GNSS single-frequency navigation at the 2014 solar maximum. *J Geod* **91**: 397–407. https://doi.org/10.1007/s00190-016-0971-0.

Park J, Veettil SV, Aquino M, Yang L, Cesaroni C. 2017. Mitigation of ionospheric effects on GNSS positioning at low latitudes: Ionospheric effect on GNSS positioning. *Navigation J Inst Navig* **64**: 67–74. https://doi.org/10.1002/navi.177.

Paziewski J. 2022. Multi-constellation single-frequency ionospheric-free precise point positioning with low-cost receivers. *GPS Solut* **26**: 23. https://doi.org/10.1007/s10291-021-01209-9.

Paziewski J. 2016. Study on desirable ionospheric corrections accuracy for network-RTK positioning and its impact on time-to-fix and probability of successful single-epoch ambiguity resolution. *Adv Space Res* **57**: 1098–1111. https://doi.org/10.1016/j.asr.2015.12.024.

Paziewski J. 2015. Precise GNSS single epoch positioning with multiple receiver configuration for medium-length baselines: methodology and performance analysis. *Meas Sci Technol* **26**: 035002. https://doi.org/10.1088/0957-0233/26/3/035002.

Paziewski J, Sieradzki R. 2020. Enhanced wide-area multi-GNSS RTK and rapid static positioning in the presence of ionospheric disturbances. *Earth Planets Space* **72**: 110. https://doi.org/10.1186/s40623-020-01238-7.

Pi X, Mannucci AJ, Lindqwister UJ, Ho CM. 1997. Monitoring of global ionospheric irregularities using the Worldwide GPS Network. *Geophys Res Lett* **24**: 2283–2286. https://doi.org/10.1029/97GL02273.

Prikryl P, Ghoddousi-Fard R, Weygand JM, Viljanen A, Connors M, Danskin DW, Jayachandran PT, Jacobsen KS, Andalsvik YL, Thomas EG, Ruohoniemi JM, Durgonics T, Oksavik K, Zhang Y, Spanswick E, Aquino M, Sreeja V. 2016. GPS phase scintillation at high latitudes during the geomagnetic storm of 17–18 March 2015: GPS Scintillation at High Latitudes. *J Geophys Res Space Phys* **121**: 10448–10465. https://doi.org/10.1002/2016JA023171.

Prikryl P, Jayachandran PT, Chadwick R, Kelly TD. 2015. Climatology of GPS phase scintillation at northern high latitudes for the period from 2008 to 2013. *Ann Geophys* **33**: 531–545. https://doi.org/10.5194/angeo-33-531-2015.

Prochniewicz D, Szpunar R, Kozuchowska J, Szabo V, Staniszewska D, Walo J. 2020. Performance of network-based GNSS positioning services in poland: a case study. *J Surv Eng* **146**: 05020006. https://doi.org/10.1061/(ASCE)SU.1943-5428.0000316.

Prochniewicz D, Szpunar R, Walo J. 2017. A new study of describing the reliability of GNSS Network RTK positioning with the use of quality indicators. *Meas Sci Technol* **28**: 015012. https://doi.org/10.1088/1361-6501/28/1/015012.

Rebischung P, Altamimi Z, Ray J, Garayt B. 2016. The IGS contribution to ITRF2014. *J Geod* **90**: 611–630. https://doi.org/10.1007/s00190-016-0897-6.

Saastamoinen J. 1973. Contributions to the theory of atmospheric refraction: Part II. Refraction corrections in satellite geodesy. *Bull Geodesique* **107**: 13–34. https://doi.org/10.1007/BF02522083.

Sato H, Jakowski N, Berdermann J, Jiricka K, Heßelbarth A, Banyś D, Wilken V. 2019. Solar radio burst events on 6 September 2017 and its impact on GNSS signal frequencies. *Space Weather* **17**: 816–826. https://doi.org/10.1029/2019SW002198.

Sieradzki R, Paziewski J. 2022. Towards a Reliable Ionospheric Polar Patch Climatology With Ground-Based GNSS. *IEEE Trans. Geosci Remote Sens.* **60**: 5802614. https://doi.org/10.1109/TGRS.2022.3149635.

Sieradzki R, Paziewski J. 2016. Study on reliable GNSS positioning with intense TEC fluctuations at high latitudes. *GPS Solut* **20**: 553–563. https://doi.org/10.1007/s10291-015-0466-0.

Sterle O, Stopar B, Pavlovčič Prešeren P. 2015. Single-frequency precise point positioning: an analytical approach. *J Geod* **89**: 793–810. https://doi.org/10.1007/s00190-015-0816-2.

Susi M, Andreotti M, Aquino M, Dodson A. 2017. Tuning a Kalman filter carrier tracking algorithm in the presence of ionospheric scintillation. *GPS Solut* **21**: 1149–1160. https://doi.org/10.1007/s10291-016-0597-y.

Vadakke Veettil S, Aquino M, Marques HA, Moraes A. 2020. Mitigation of ionospheric scintillation effects on GNSS precise point positioning (PPP) at low latitudes. *J Geod* **94**: 15. https://doi.org/10.1007/s00190-020-01345-z.

van der Meeren C, Oksavik K, Lorentzen D, Moen JI, Romano V. 2014. GPS scintillation and irregularities at the front of an ionization tongue in the nightside polar ionosphere. *J Geophys Res Space Phys* **119**: 8624–8636. https://doi.org/10.1002/2014JA020114.

Villiger A, Schaer S, Dach R, Prange L, Sušnik A, Jäggi A. 2019. Determination of GNSS pseudo-absolute code biases and their long-term combination. *J Geod* **93**: 1487–1500. https://doi.org/10.1007/s00190-019-01262-w.

Wang J, Stewart MP, Tsakiri M. 1998. A discrimination test procedure for ambiguity resolution on-the-fly. *J Geod* **72**: 644–653. https://doi.org/10.1007/s001900050204.

Wang Y, Zhang Q-H, Jayachandran PT, Lockwood M, Zhang S-R, Moen J, Xing Z-Y, Ma Y-Z, Lester M. 2016. A comparison between large-scale irregularities and scintillations in the polar ionosphere. *Geophys Res Lett* **43**: 4790–4798. https://doi.org/10.1002/2016GL069230.

Wanninger L. 2004. Ionospheric disturbance indices for RTK and network RTK positioning. In: Presented at the Proceedings of the 17th International Technical Meeting of the Satellite Division of The Institute of Navigation (ION GNSS 2004), Long Beach, CA, pp. 849–2854.

Wielgosz P, Kashani I, Grejner-Brzezinska D. 2005. Analysis of long-range network RTK during a severe ionospheric storm. *J Geod* **79**: 524–531. https://doi.org/10.1007/s00190-005-0003-y.

Wu JT, Wu SC, Hajj GA, Bertiger WI, Lichten SM. 1992. Effects of antenna orientation on GPS carrier phase. *Astrodynamics* **1991**: 1647–1660.

Xu R, Liu Z, Chen W. 2015. Improved FLL-assisted PLL with in-phase pre-filtering to mitigate amplitude scintillation effects. *GPS Solut* **19**: 263–276. https://doi.org/10.1007/s10291-014-0385-5.

Yang Z, Morton YTJ, Zakharenkova I, Cherniak I, Song S, Li W. 2020. Global View of ionospheric disturbance impacts on kinematic GPS positioning solutions during the 2015 St. Patrick's Day Storm. *J Geophys Res Space Phys* **125**: e2019JA027681. https://doi.org/10.1029/2019JA027681.

Yunck T. 1996. Orbit determination. In: *Global Positioning System—Theory and Applications*. Parkinson BW, Spilker JJ, (Eds.), AIAA: Washington DC, USA.

Zhang B, Teunissen PJG, Yuan Y, Zhang H, Li M. 2018. Joint estimation of vertical total electron content (VTEC) and satellite differential code biases (SDCBs) using low-cost receivers. *J Geod* **92**: 401–413. https://doi.org/10.1007/s00190-017-1071-5.

Zhao C, Zhang B, Zhang X. 2021. SUPREME: an open-source single-frequency uncombined precise point positioning software. *GPS Solut* **25**: 86. https://doi.org/10.1007/s10291-021-01131-0.

Cite this article as: Paziewski J, Høeg P, Sieradzki R, Jin Y, Jarmolowski W, et al. 2022. The implications of ionospheric disturbances for precise GNSS positioning in Greenland. *J. Space Weather Space Clim.* **12**, 33. https://doi.org/10.1051/swsc/2022029.